

Photon transport enhanced by transverse Anderson localization in disordered superlattices

P. Hsieh^{1,2*}, C. Chung^{2,3}, J. F. McMillan¹, M. Tsai^{2,4}, M. Lu⁵, N. C. Panoiu^{6,7}, and C. W. Wong^{1,8*}

¹Optical Nanostructures Laboratory, Center for Integrated Science and Engineering, Solid-State Science and Engineering, Mechanical Engineering, Columbia University, New York, NY 10027, USA

²Quantumstone Research Inc., Taipei 114, Taiwan

³Center for Micro/Nano Science and Technology and Advanced Optoelectronic Technology Center, National Cheng Kung University, Tainan 701, Taiwan

⁴Center for Measurement Standards, Industrial Technology Research Institute, Hsinchu 300, Taiwan

⁵Center for Functional Nanomaterials, Brookhaven National Laboratory, Upton, NY 11973, USA

⁶Department of Electronic and Electrical Engineering, University College London, Torrington Place, London WC1E 7JE, UK

⁷Thomas Young Centre, London Centre for Nanotechnology, University College London, 17-19 Gordon Street, London, WC1H 0AH, UK

⁸Mesoscopic Optics and Quantum Electronics Laboratory, University of California, Los Angeles, CA 90095, USA

* Correspondence and requests for materials should be addressed to P.H., N.C.P or C.W.W. (email: ph2285@columbia.edu; n.panoiu@ucl.ac.uk; cheewei.wong@ucla.edu)

I. Schematic representation of a superlattice with 3 superperiods

A schematic representation of a photonic superlattice with 3 superperiods is shown in Figure S1. Superlattices consist of alternating layers of hexagonal photonic crystals (PhCs) and slabs of homogeneous material [SR1]. The hexagonal PhC and the photonic superlattice have different symmetry properties, and consequently they have different first Brillouin zones, as illustrated in Figure S1.

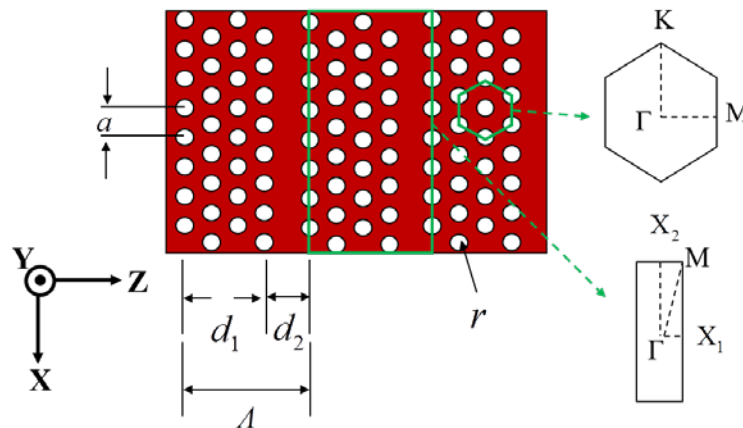


Figure S1 | Schematic representation of the photonic superlattice. First Brillouin zones for both the hexagonal photonic crystal lattice and photonic superlattices. a is the lattice period of the photonic crystal, r is the radius of the air holes, d_1 is the length of the photonic crystal layer, d_2 is the length of the homogeneous silicon slab, and $\Lambda = d_1 + d_2$ is the period of the photonic superlattice. In our design, the photonic crystal parameters are $a = 500$ nm, $r/a = 0.29$, $d_2/d_1 = 0.18$, and the silicon device thickness of the silicon-on-insulator wafer $t = 320$ nm. In all our fabricated devices, the PhC sections of the superlattice contain 7 lattice periods in the longitudinal direction (z -axis, which coincides with the Γ -M symmetry axis of the PhC).

II. Design of structural disorder and hole distribution in the superlattice

Structural disorder of the photonic superlattice is introduced by the perturbation of PhC holes with heptagonal, square, and triangular shapes. In particular, the scatterer (hole) shape is designed such that the circular hole coincides with the inscribed circle of the heptagonal and square scatterers, as shown in Figure S2.

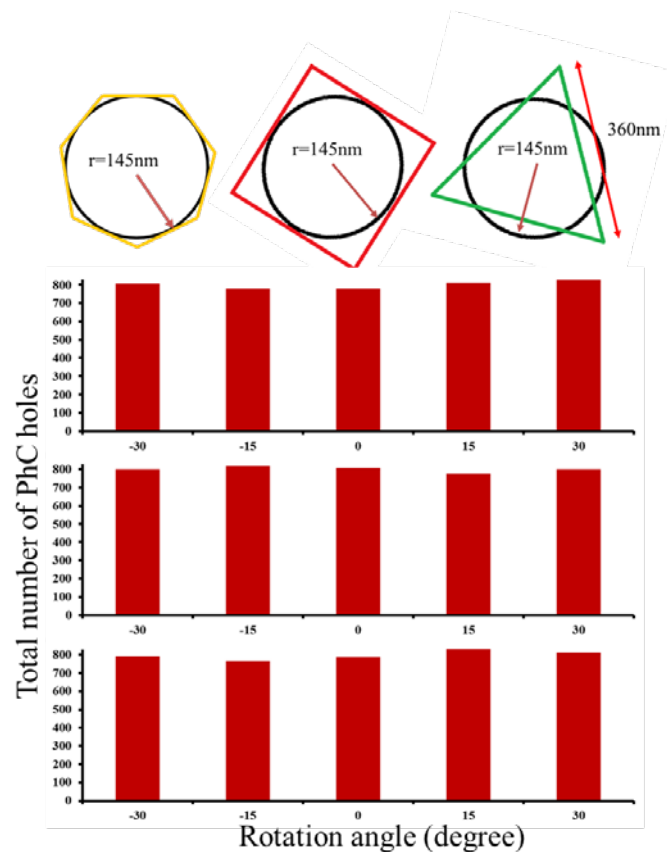


Figure S2 | Schematic representation of the disordered scatterers (top inset) and the stochastically-uniform distributions of the random rotations. From top to bottom, the panels correspond to the heptagonal-hole, square-hole, and triangular-hole superlattices.

For the triangular scatterer, we choose the edge size to be 360 nm for each side so that the area of the circular and the triangular holes are approximately equal. All the air hole scatterers are rotated by 0° , 15° , -15° , 30° , or -30° , with the angle of rotation described by a stochastically-uniform random distribution. The distributions for the three families of scatterers are shown in Figure S2. The disorder distribution level is defined by the standard deviation of the total number of the rotation angles, which can be found as $\sim 21.3^\circ$, $\sim 21.2^\circ$, and $\sim 21.2^\circ$ for the heptagonal-hole superlattice (HHS), square-hole superlattice (SHS), and triangular-hole superlattice (THS), respectively. We note that using a finite, discrete set of rotation angles is enough to introduce structural disorder in our photonic system. In Figure S3 we present the focused ion beam images of the resulting fabricated nanostructured superlattices (see Methods on nanofabrication parameters). In all cases the centers of the holes form a hexagonal lattice, within the positional accuracy of the electron-beam lithography writer.

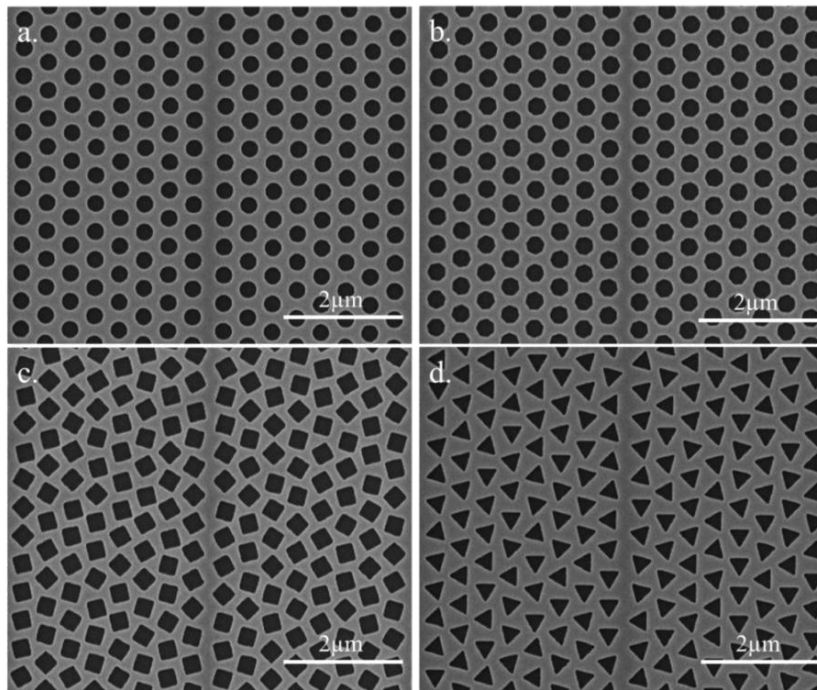


Figure S3 | Focus ion beam images of photonic crystal superlattices with different scatterer shape. a, circular-hole superlattice. **b,** heptagonal-hole superlattice. **c,** square-hole superlattice. **d,** triangular-hole superlattice.

An additional type of disorder is introduced if the size of the holes is set in the domain $(r-\Delta r/2, r+\Delta r/2)$, where r is the radius of the circular hole, and Δr is the distance from each point on the boundary of the heptagonal, square, and triangular holes to the center of the circular hole. The level of structural disorder can then be further characterized by the averaged deviation of Δr from the circular hole radius r , averaged over 600 holes. Under these conditions, the structural disorder is determined to be $\sim 2\%$, $\sim 6\%$, and $\sim 13\%$ for the HHS, SHS, and THS, respectively.

III. Band diagrams, equifrequency surfaces, effective indices of refraction for the PhC and the homogeneous slab, and guiding resonances of the transverse PhC waveguides

The photonic band structures of the underlying PhC with hexagonal symmetry (see Figure S4a) as well as that of the photonic superlattice are computed by using RSoft's BandSOLVE, a commercially available software that implements a numerical algorithm based on the plane wave expansion of the electromagnetic field and spatial distribution of the dielectric constant of the photonic structure. For 1D approximations, cascaded 2×2 transmission matrices

through the PhC and the homogeneous regions can also be used. In all our three-dimensional (3D) numerical calculations of the photonic bands a convergence tolerance of 10^{-8} is enforced. The photonic bands of the PhC are classified based on their parity symmetry with respect to a plane crossing through the middle of the silicon slab, whose normal is along the y -axis, into TM-like (odd) and TE-like (even) modes. In particular, at the location of this plane the electric (magnetic) field of the TM-like (TE-like) mode is predominantly perpendicular onto the plane.

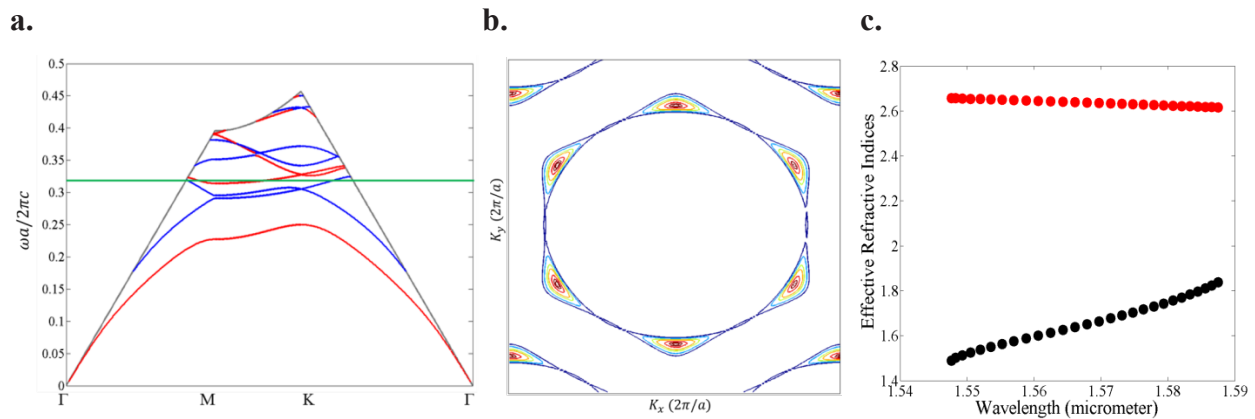


Figure S4 | Band structure, equifrequency curves, and effective mode refractive indices of the hexagonal photonic crystal. **a**, Guided mode band structure computed using a plane-wave expansion method, with the red (TE-like) and blue (TM-like) modes. The photonic crystal parameters are $a = 500$ nm, $r = 145$ nm, and $t = 320$ nm. **b**, Equifrequency curves of the photonic crystal. The weak anisotropy of the flat sections of the equifrequency curves leads to the observed collimation effect. **c**, Effective refractive indices of the second TM-like photonic crystal band (black) and the silicon slab (red), show all-positive refraction of the superlattice.

The equifrequency surfaces are determined from the band structure, and represent guided photonic modes of the PhC that correspond to a constant frequency. The equifrequency curves shown in Figure S4b illustrate that within a certain frequency range optical beams can only propagate in a narrow interval of angles, centered around the Γ -M direction. This weak anisotropy contributes to the observed collimation effect. The effective refractive indices corresponding to the second TM-like band (Figure S4c) are determined from the relation $k = \omega|n|/c$, with k in the first Brillouin zone.

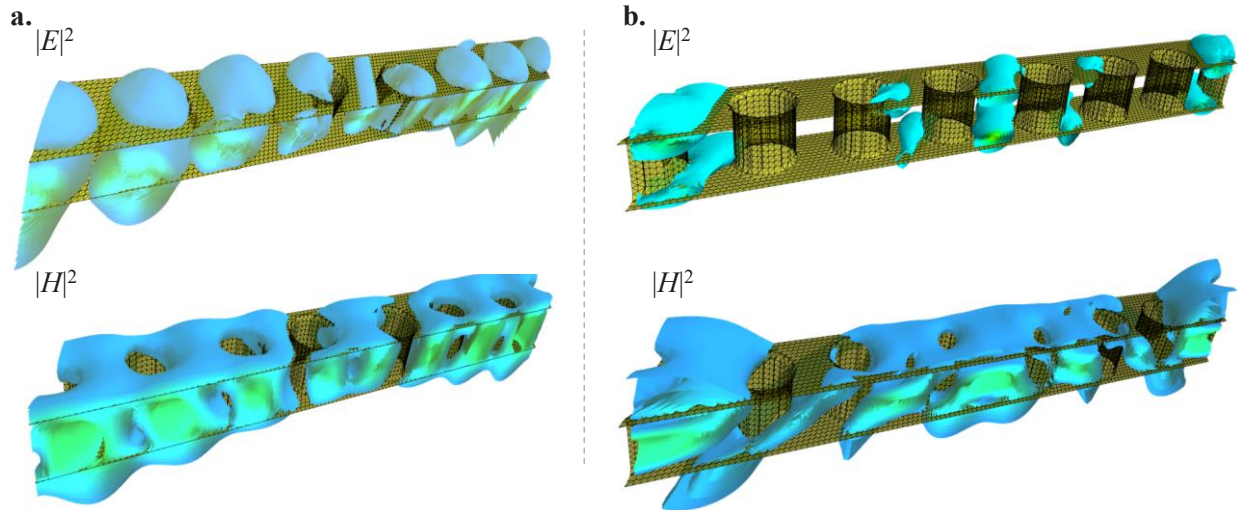


Figure S5 | $|E|^2$ -field and $|H|^2$ -field distributions of the guided modes of the photonic crystal superlattice, calculated at the Γ symmetry point. The modes correspond to a wavelength of 1529 nm (a) and 1590 nm (b). For a clearer visualization, the field profiles are presented as a set of isosurfaces corresponding to increasing values of $|E|^2$ and $|H|^2$. For clarity, the dielectric matrix of the photonic crystal is superimposed onto the field distributions

Figure S5 shows the computed spatial distribution of the electric field ($|E|^2$) and magnetic field ($|H|^2$) intensities of the guiding resonances (leaky modes) corresponding to the two flat bands (with normalized frequency near 0.314 and 0.327) illustrated in the zoomed-in band structure of Figure 1f in the main text. At the Γ symmetry point ($k_x=0$) these two modes are embedded in the radiation continuum of the PhC slab waveguide and represent guided resonances excited in the transverse 1D PhC waveguides.

IV. Finite difference time domain simulation and calculation of the effective beam width

The numerical simulations of the intensity field distribution have been performed with MEEP, a freely available code based on the finite-difference time-domain (FDTD) method [SR2]. In all numerical simulations we used a uniform computational grid of 33 grid points per micrometer. This choice ensures that the smallest characteristic length of the system (in our case, the diameter of the holes) contains at least 10 grid points, allowing sufficient numerical accuracy in all our cases concerning dielectric structures. In our numerical simulations we used a pulsed excitation source with a 1550 nm central wavelength with a spectral full-width half-maximum of 90 nm.

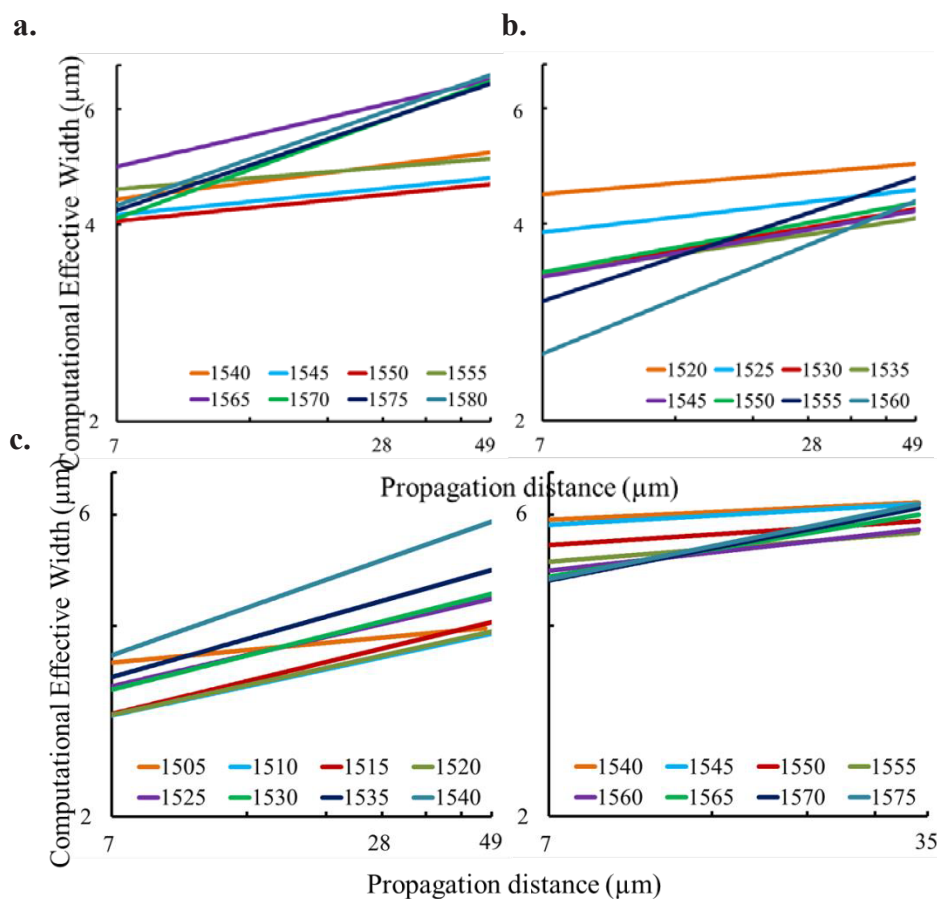


Figure S6 | Log-log plots of the simulated effective beam width versus the propagation distance. Summary for circular-hole superlattice (a), heptagonal-hole superlattice (b), square-hole superlattice (c), and triangular-hole superlattice (d).

The computed effective beam widths, $\omega_{eff}(z)$, for the different superlattice, propagation distance z , and wavelength, are summarized in Figure S6. The physical nature of the beam

divergence process is revealed by the slope of $\omega_{effc}(z)$ when represented in log-log scale. The log-log plot of the computationally determined beam width $\omega_{effc}(z)$ for the CHS shows the slope $\nu \sim 0.05$ from 1545 nm to 1555 nm. In the presence of $\sim 2\%$ (HHS), $\sim 6\%$ (SHS), and $\sim 13\%$ (THS) disorder, the log-log plot of $\omega_{effc}(z)$ shows a significantly different spectral dependence of the slope ν (see main text).

In particular, for the HHS from 1525 nm to 1550 nm, $\nu \sim 0.05$ to 0.1. For the SHS from 1505 nm to 1530 nm, $\nu \sim 0.05$ to 0.1. For the THS from 1540 nm to 1575 nm, $\nu \sim 0.05$ to 0.1. This illustrates that the collimation bandwidth increases when structural disorder is added to the system, in agreement with the experimental results described in the main text.

V. Analysis of the measured collimation and spatial full-width half-maximum in the periodic and disordered superlattices

Figures S7 to S10 represent several measured far-field infrared images related to the Figures 4d to 4g in the main text. Measurements are taken from 1530 nm to 1620 nm with 100 pm resolution, with hundreds of gigabytes of data collected through a fast data acquisition card. The effects of laser speckle is also analyzed by averaging over 20 images, each taken at 1 pm spectral resolution apart, with no significant difference from the raw data below.

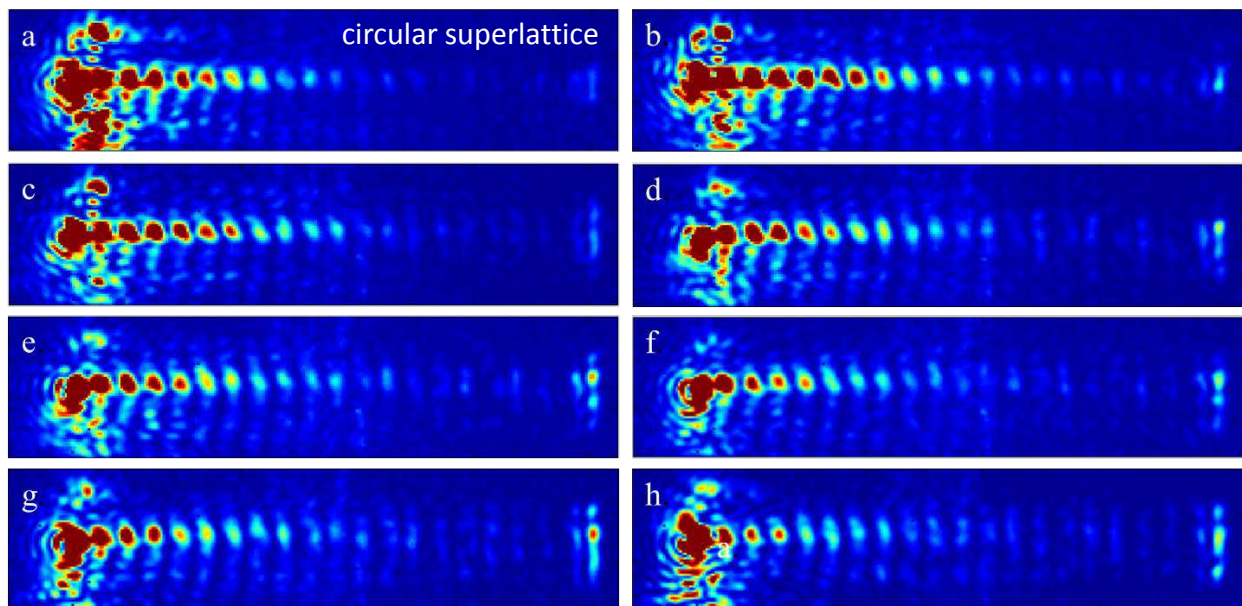


Figure S7 | Measured far-field infrared images of the circular-hole superlattice. a through h, at 1546 nm, 1550 nm, 1554 nm, 1558 nm, 1561 nm, 1564 nm, 1567 nm, and 1571 nm, respectively. Beam propagation is from left to right.

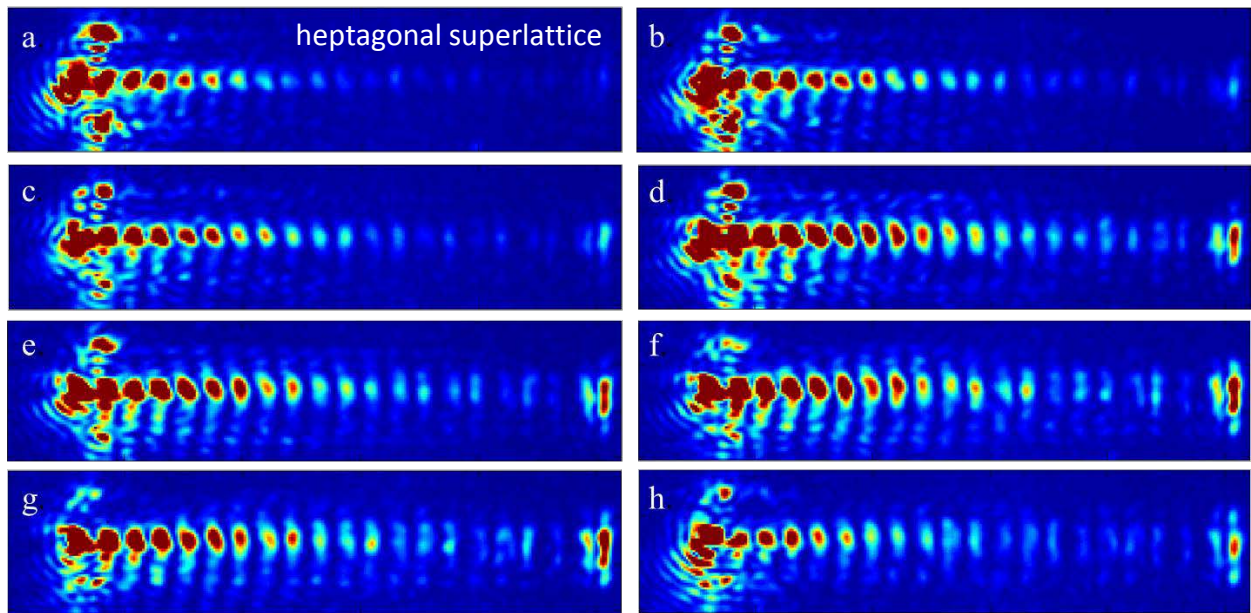


Figure S8 | Measured far-field infrared images of the heptagonal-hole superlattice. a through h, at 1546 nm, 1550 nm, 1554 nm, 1558 nm, 1561 nm, 1564 nm, 1567 nm, and 1571 nm, respectively. Beam propagation is from left to right.

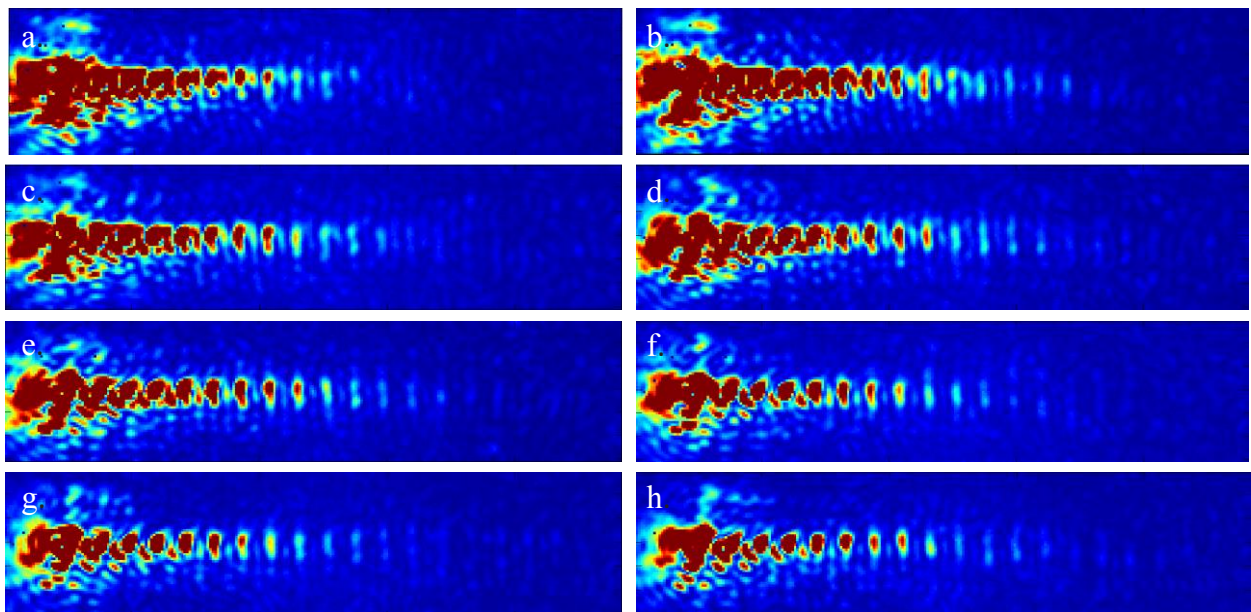


Figure S9 | Measured far-field infrared images of the square-hole superlattice. a through h, at 1551 nm, 1555 nm, 1559 nm, 1563 nm, 1566 nm, 1569 nm, 1572 nm, and 1576 nm, respectively. Beam propagation is from left to right.

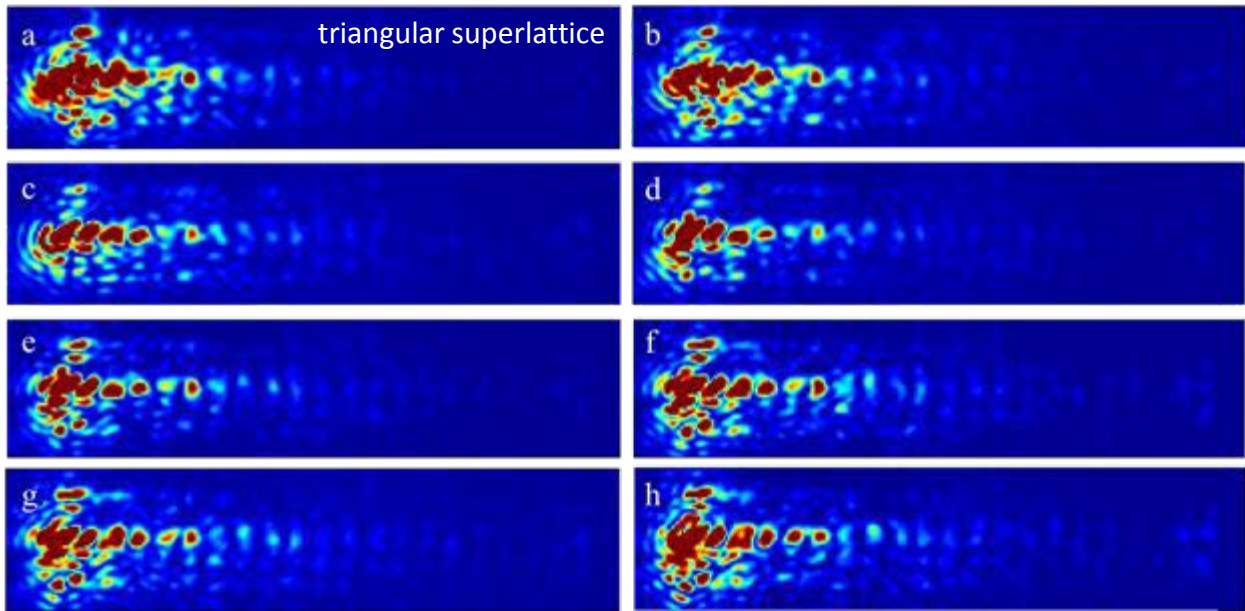


Figure S10 | Measured far-field infrared images of the triangular-hole superlattice. a through h, at 1576 nm, 1580 nm, 1584 nm, 1588 nm, 1591 nm, 1594 nm, 1597 nm, and 1601 nm, respectively. Beam propagation is from left to right.

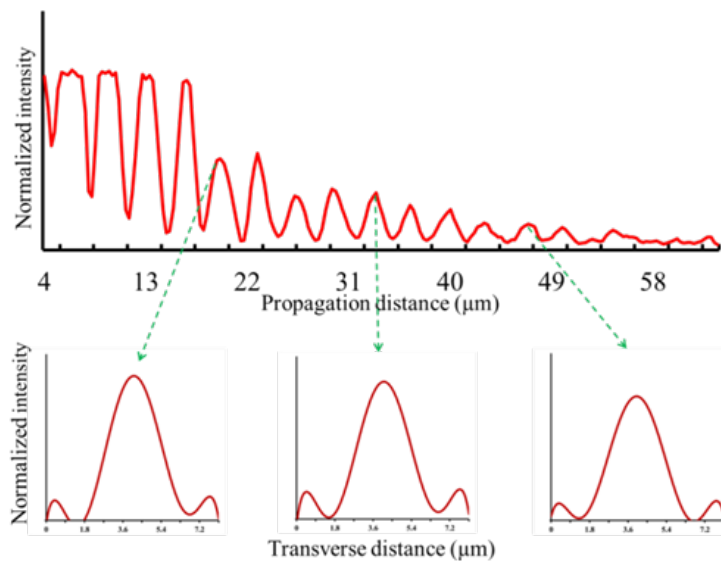


Figure S11| Intensity distribution along the propagation distance (z -axis) at 1550 nm. The top plot shows the z -dependence of the intensity distribution for the circular-hole superlattice, whereas examples of the intensity distribution along the transverse distance (x -axis), at several locations along the z -axis, are presented in the bottom panels.

The full-width at half-maximum (FWHM) of the collimating beams are determined at all maxima intensity locations along the superlattice, as shown in Figure S11 (circular superlattice shown). For the disordered superlattices (HHS, SHS, and THS), the transverse spatial profile is best matched with an exponential decay instead of a Gaussian profile, further supporting the evidence of transverse localization. Next, the beam FWHM versus the propagation distance is represented on log-log scale and linear fitting is used to determine the corresponding slope, as per Figures 4d to 4g in the main text. More specifically, from the asymptotic dependence of the beam width it is found that ω_{FWHM} is of the form $\omega_{FWHM}(z) \propto z^\nu$, where ν is a power exponent whose value was calculated to be in the range $\nu < 0.5$. This is compared to the calculated effective width versus propagation distance determined from FDTD simulations in Figure S6.

In addition, the collimating beam profile shows transverse symmetry as per Figure S12, from both the numerical simulations and measurements. From the 3D simulations, with increasing disorder the transverse asymmetry is larger. The beam profile asymmetry is observed in the measurements as well, with several examples presented here. Note that the measurements and simulations correspond to different structural disorder realizations and therefore the particular field profiles should not be directly compared.

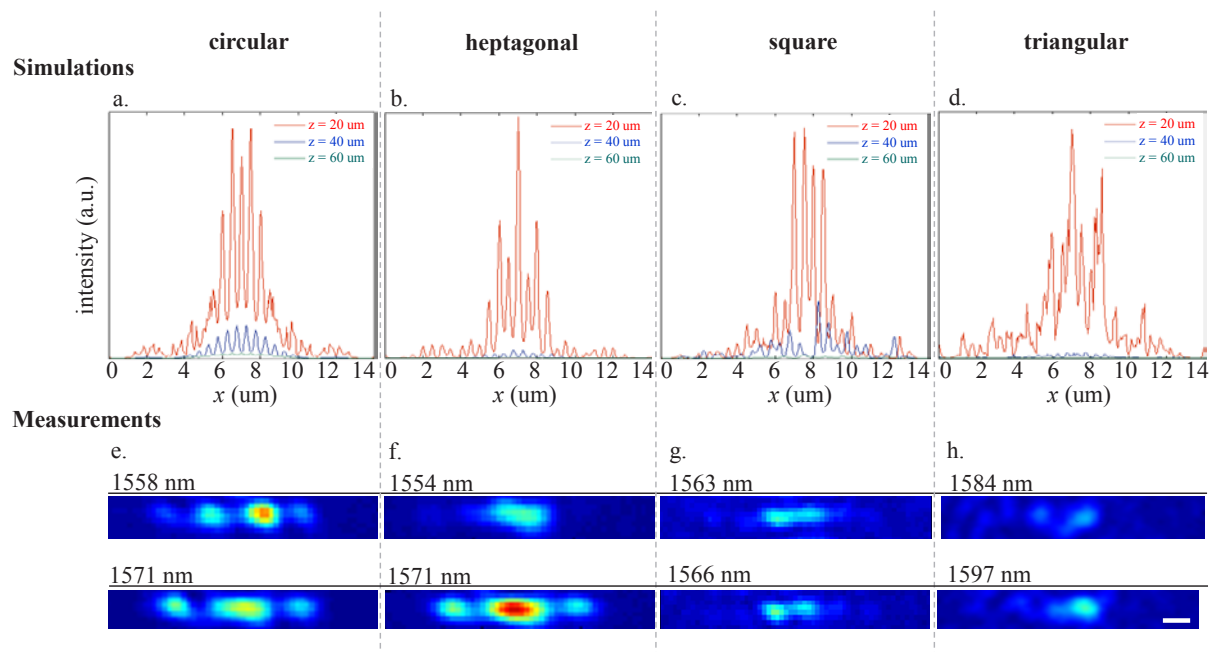


Figure S12 | Asymmetric transverse beam profiles for the CHS, HHS, SHS and THS superlattices, determined both from the numerical simulations and measurements. In the simulations, the wavelengths are 1550 nm (CHS), 1530 nm (HHS), 1515 nm (SHS), and 1550

nm (THS), and correspond to the maximum observed collimation. In the measurements, the example wavelengths are indicated at the top left of the panels, each taken at the output or near the output. Scale bar: 2 μm .

VI. Near-field scattering imaging finer feature of collimation:

The near-field scanning optical microscope used to examine the optical near-field is a Veeco Aurora-3, a commercial and aperture-type near-field scanning optical microscope.

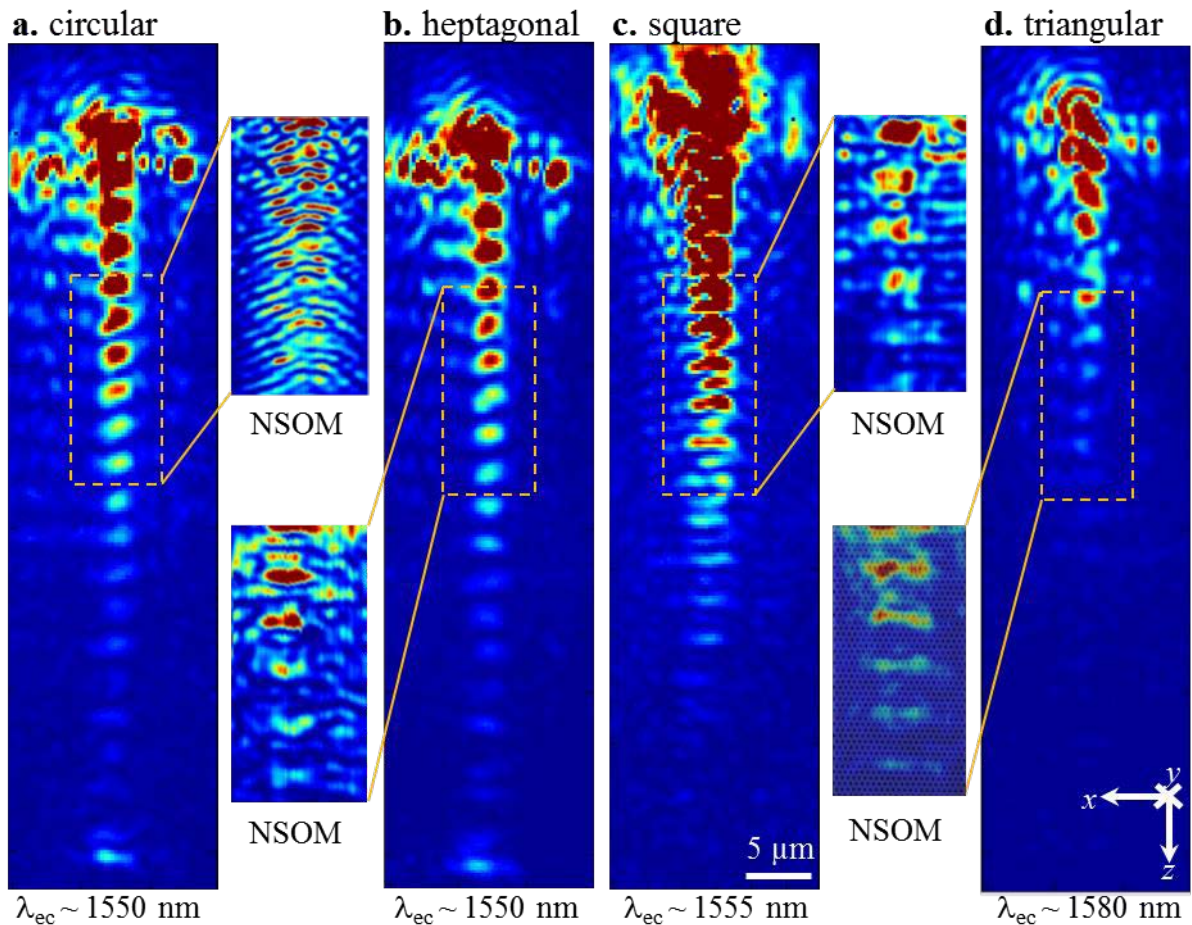


Figure S13 | Far- and near-field infrared scattering images illustrating the wavelength dependent beam collimation. **a**, Circular-hole superlattice at 1550 nm. **b**, heptagonal-hole superlattice at 1550 nm. **c**, square-hole superlattice at 1555 nm. **d**, triangular-hole superlattice at 1580 nm. The primary image represents the far-field, with the zoomed insets being extracted from the near-field scanning optical microscopy images.

The near-field probe was produced by using of thermal pulling method to create ~ 150 nm apertures and the tip was coated with a 100 nm aluminum layer for light confinement. The near-field probe was then attached to a tuning fork sensor produced by Veeco Instruments/Bruker AFM for constant-distance scanning. The piezoelectric scanner of near-field scanning optical microscope was calibrated by a periodic grid sample in topography image mode to ensure the accuracy of the measurements. To couple light into the optical chip, a UV-curing adhesive was used to bond a tapered lens fiber to the silicon input waveguide, with stable attachment. Beam propagation through the superlattices was observed with the near-field microscope and the Santec TSL-510 tunable laser used to obtain the spectral character. Detection was performed with a New Focus 2153 InGaAs femtowatt photoreceiver with ~ 23 fW/Hz^{1/2} noise equivalent power.

VII. Disordered anisotropic medium with flat spatial dispersion curves

In order to investigate the transverse light localization in the superlattice, we also nanofabricated and examined a set of anisotropic artificial mediums, with the collimation mechanism of flat spatial dispersion surfaces studied in earlier works (Refs. 6-8 in main text). These anisotropic artificial media were based on a square lattice design, with the device size of a few hundred micrometers. The PhC hole-to-lattice ratio $r/a = 0.305$, with lattice period $a = 360$ nm. Figure S14a shows equifrequency curves for the second TE band of the PhC, with the relevant contours near the wavelengths of interest. For the normalized frequency $\omega = 0.2236$, whose equifrequency curve is represented in Fig. S14 by the red contour, the PhC shows remarkably small spatial dispersion (weak anisotropy), which suggests beam collimation. This wavelength, at which the collimation is most effective, is denoted by λ_{ec} .

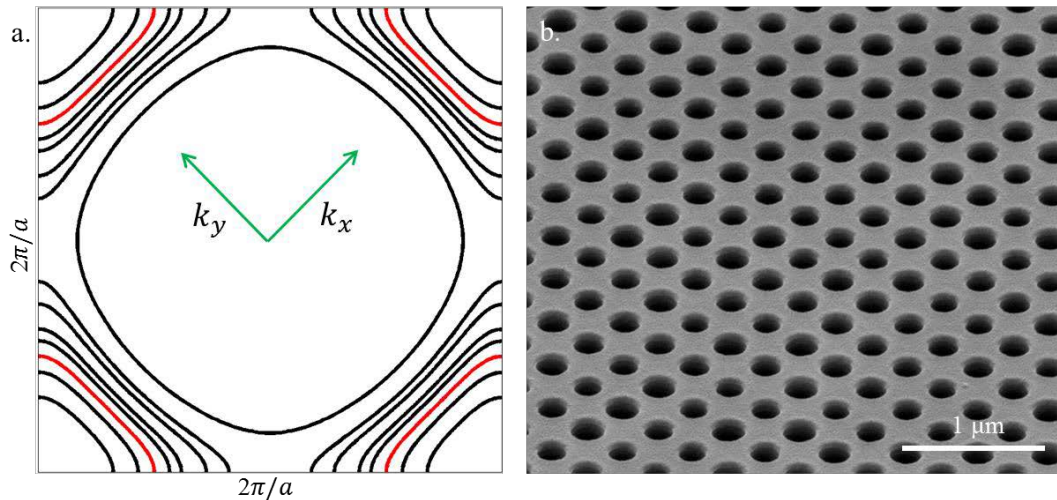


Figure S14 | Photonic crystals as anisotropic media. **a**, computed equipfrequency surface of the periodic photonic crystals. Red curves correspond to the normalized frequency $\omega=0.2236$, which leads to most effective collimation. **b**, example of nanofabricated photonic crystal with highest level of disorder, imaged through focused ion beam.

To introduce disorder in this photonic system, three other disordered structures were also designed and fabricated, with different levels of perturbation of the PhC holes. For each level of disorder, the radius of the hole was described by a uniform random distribution with different width. The three layouts of disordered PhC were subsequently generated by using these random distribution functions and prepared for fabrication. The lattice period of all the disordered PhC was the same, $a=360$ nm, so as a reliable comparison of the beam propagation in the PhCs can be made. Figure S15 shows the radius distribution corresponding to the three levels of disorder, from the lowest (Fig. S15a) to the highest (Fig. S15c) disorder level.

Using the method described in main text, the cleaved nanofabricated chip was mounted on the sample holder. Then a TE-polarized optical beam was coupled into the PhC via a focus lens, this process being repeated 10 times. In each of these 10 measurements, the coupling point was randomly shifted in the horizontal direction of the device, to ensure that the results are not dependent on a specific termination profile of the PhC.

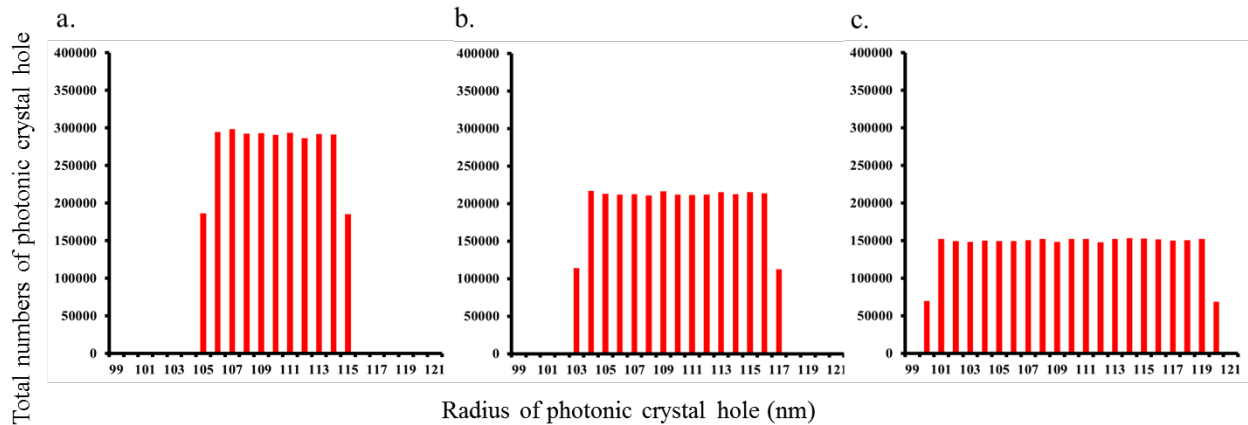


Figure S15 | Distribution of the hole radius for different levels of disorder in a PhC based anisotropic medium. a, low level of disorder. **b**, medium level of disorder. **c**, high level of disorder.

VIII. Transmission spectrum and group-velocity delay further evidencing the relation between the excitation of transverse guided modes and the observed collimation

Furthermore we performed group velocity delay and transmission spectra measurements of the superlattices. For the precision amplitude and phase measurements, coherent swept wavelength interferometry is implemented, with 500 fm wavelength precision and time delays of up to a few nanoseconds.

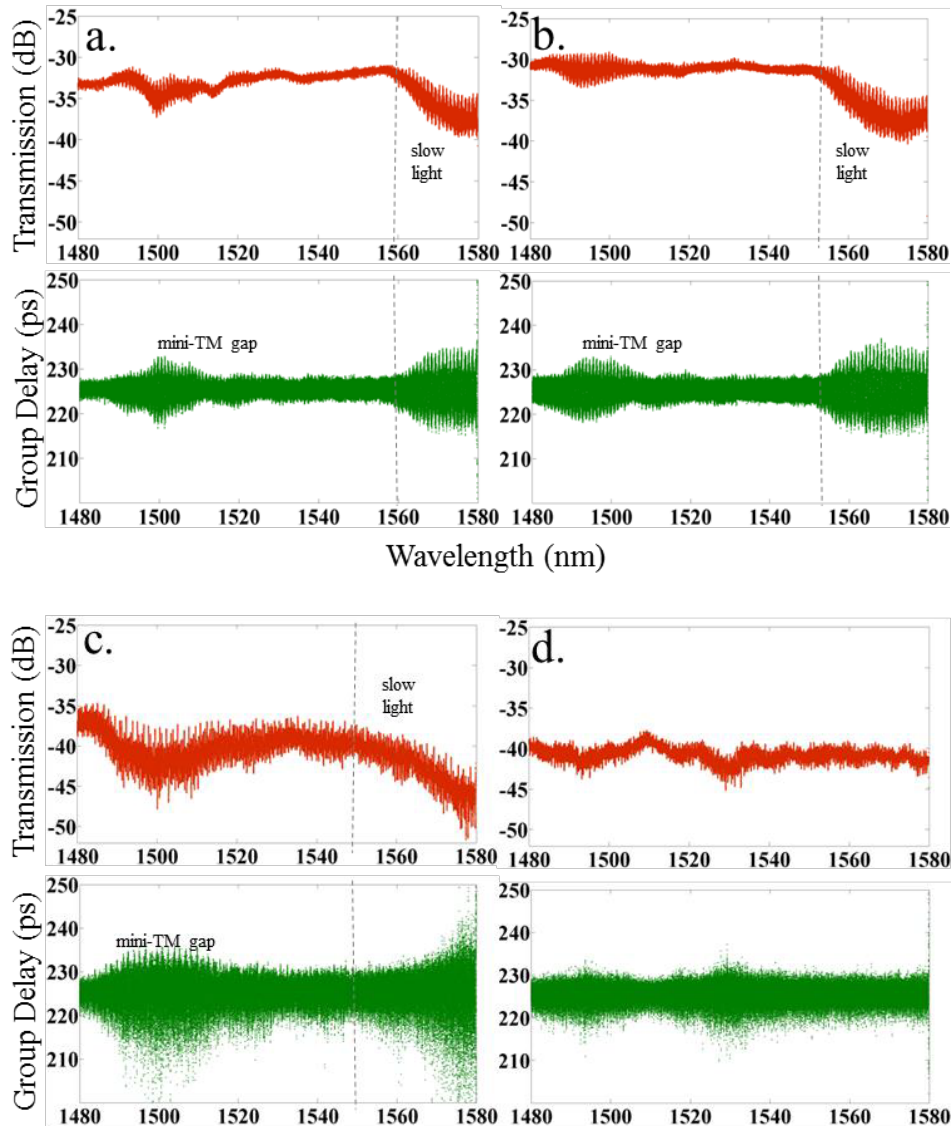


Figure S16 | Transmission spectra and group velocity delay of the circular-hole superlattice (a), with slow-light regime for wavelengths larger than ~ 1560 nm. A mini-transverse-magnetic gap around 1500 nm arises from the higher-order modes. **b**, heptagonal-hole, **c**, square-hole, and **d**, triangular-hole superlattice.

The interferometry is performed in a dual-stage fiber interferometer with absolute hydrogen cyanide $\text{H}^{13}\text{C}^{14}\text{N}$ gas cell reference of the $2\nu_3$ rotational-vibrational absorption lines, with optimized power in the local oscillator. We also note that the group-delay measurements are taken relative to an input delay, a constant value of which is uniformly used for all superlattices for comparison. Shorter superlattices (of 5 superperiods) are also used in the transmission measurements to provide sufficient transmission signal for accurate measurements, as shown in

Figure S13. The transmission spectrum and group velocity delay of each device are measured experimentally within the spectral range of 1480 nm to 1580 nm.

Slow-light band edges are observed to occur concurrently near the wavelengths of most effective collimation λ_{ec} , and away from the higher-order transverse-magnetic mini-gap around 1500 nm. In the regular CHS superlattices, this slow-wave propagation arises due to z -cascaded evanescently coupled transverse guided modes, further evidencing the relation between the transverse guided mode excitation and the observed CHS collimation.

Supplementary References:

[SR1] Kocaman, S., Aras, M. S., Hsieh, P., McMillan, J. F., Biris, C. G., Panoiu, N. C., Yu, M. B., Kwong, D. L., Stein, A., & Wong, C. W. Zero phase delay in negative-refractive-index photonic crystal superlattices. *Nature Photonics* **5**, 499 (2011).

[SR2] Oskooi, A. F., Roundy, D., Ibanescu, M., Bermel, P., Joannopoulos, J. D., & Johnson, S. G. MEEP: A flexible free-software package for electromagnetic simulations by the FDTD method, *Computer Physics Communications* **181**, 687 (2010).